

Quantitative Benchmarking of Anomaly Detection Methods in Digital Pathology

Can Cui

Department of Computer Science
Vanderbilt University, TN, USA

Xindong Zheng

Department of Computer Science
Vanderbilt University, TN, USA

Ruining Deng

Department of Radiology
Weill Cornell Medicine, NY, USA

Quan Liu

Department of Computer Science
Vanderbilt University, TN, USA

Tianyuan Yao

Department of Computer Science
Vanderbilt University, TN, USA

Keith T Wilson

Department of Medicine
Vanderbilt University Medical Center, TN, USA
Veterans Affairs Tennessee Valley
Healthcare System TN, USA

Lori A Coburn

Department of Medicine
Vanderbilt University Medical Center
Veterans Affairs Tennessee Valley
Healthcare System TN, USA

Bennett A Landman

Department of Electrical and
Computer Engineering
Department of Computer Science
Vanderbilt University, TN, USA

Haichun Yang

Department of Pathology, Microbiology,
and Immunology
Vanderbilt University Medical Center, TN, USA

Yaohong Wang

Department of Anatomical Pathology
UT MD Anderson Cancer Center, TX, USA

Yuankai Huo

Department of Computer Science
Department of Electrical and Computer Engineering
Vanderbilt University, TN, USA
★ Corresponding Author

Abstract—Anomaly detection has been widely studied in the context of industrial defect inspection, with numerous methods developed to tackle a range of challenges. In digital pathology, anomaly detection holds significant potential for applications such as rare disease identification, artifact detection, and biomarker discovery. However, the unique characteristics of pathology images—such as their large size, multi-scale structures, stain variability, and repetitive patterns—introduce new challenges that current anomaly detection algorithms struggle to address. In this quantitative study, we benchmark over 20 classical and prevalent anomaly detection methods through extensive experiments. We curated five digital pathology datasets—both real and synthetic—to systematically evaluate these approaches. Our experiments investigate the influence of image scale, anomaly pattern types, and training epoch selection strategies on detection performance. The results provide a detailed comparison of each method’s strengths and limitations, establishing a comprehensive benchmark to guide future research in anomaly detection for digital pathology images.

I. INTRODUCTION

Anomaly detection refers to a model’s ability to identify deviations from the learned distribution of training data during inference. These models are typically trained solely on normal data but distinguish between normal and abnormal data during inference, which is categorized as unsupervised/semi-supervised anomaly detection [1], [2]. This paradigm is particularly suitable for scenarios where normal data is abundant, while anomalies are rare, difficult to obtain during training,

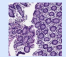




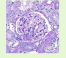
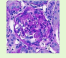
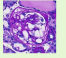

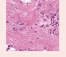

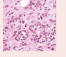
Pathology Images			Applications
Characteristics	Normal	Abnormal	
Scale variation	 	 	Rare Disease Detection
Stain variety	 	 	Lesion Localization
Repetitive patterns	 	 	Artifact Detection
...

Fig. 1. **Key characteristics and clinical applications of anomaly detection in digital pathological images.** Compared to natural images, anomaly detection in pathological images has the following characteristics: 1) Greater scale variation in multiscale, including cells and tissues. 2) Diversity in staining, such as differences in staining intensity and imaging brightness. 3) Repetitive patterns, with blurry boundaries between normal and abnormal.

or highly variable with unknown manifestations. Anomaly detection has been widely applied in real-world tasks, including defect detection in manufacturing, abnormal event recognition in surveillance videos, and fraud detection in financial transactions.

Anomaly detection also has potential applications in the

field of medical imaging. Pathology images are typically large-scale, with normal samples readily available from healthy individuals. Lesion areas are often small relative to normal regions, exhibit high pattern variability with unclear boundaries, and are rarely annotated by experts [3]. Additionally, privacy concerns may limit the availability of certain patient data, and some lesions may be extremely rare or entirely novel. By training only on normal data, anomaly detection can enable automatic lesion identification, with pixel-wise or patch-wise anomaly scores enhancing interpretability in disease diagnosis. Also, anomaly detection plays a crucial role in preclinical research, such as identifying the toxicological effects of candidate drugs [4], [5]. Given the diverse manifestations of pathological abnormalities, supervised classification datasets often fail to capture all possible variations. In contrast, the availability of large-scale normal data allows anomaly detection methods to generalize to unseen anomalies in pathology images, enabling robust and broad applications.

However, pathology images differ significantly from radiology and natural images, posing unique challenges for anomaly detection Fig. 1. For example, pathology image analysis requires multi-scale interpretation, as pathologists frequently zoom in and out to capture both local and global diagnostic information. Staining variation also introduces additional complexity, requiring models to exhibit robustness to these differences [4]. Furthermore, pathology images often contain repetitive patterns, while anomalous regions tend to be highly complex and diverse, reducing the effectiveness of conventional anomaly detection algorithms. Therefore, we aim to evaluate the performance of general anomaly detection methods on pathology images.

This quantitative study focuses on benchmarking anomaly detection in pathology images. We summarize prior work, comprehensively benchmark 23 anomaly detection methods on real digital pathology images and synthetic datasets, and discuss the challenges and future directions in this field. The contributions of this work are summarized as follows:

- We benchmark 23 classic and state-of-the-art anomaly detection methods on synthetic and real digital pathology images, featuring distinct anomaly patterns for comprehensive evaluation.
- Our experiments explore the impact of key components on anomaly detection performance in digital pathology, including image scale, reversed anomaly patterns, and strategies for selecting training epochs, which are rarely discussed in previous studies.
- We review the application of existing anomaly detection methods to pathology images and, combined with our experimental results, provide valuable insights to guide future research in this field.

II. RELATED WORK

Several reviews summarize anomaly detection in industrial device images [1], [6], [7]. In recent years, there have been some review papers focused on anomaly detection in medical

imaging [8]–[10]. The most recent one, Cai et al [8], benchmarked several medical datasets with different modalities and conducted extensive experiments to analyze the characteristics of different methods, including the impact of pretrained weights, loss functions, and key hyperparameter settings. Similarly, Lagogiannis et al. [9] and Bao et al [10] also benchmarked anomaly detection methods on various medical images and experimentally examined the factors such as pretrained weights, the size of the dataset, model efficiency, etc. In our work, we selected a set of widely adopted methods from recent years in both industrial and medical image anomaly detection. These include methods from two publicly available GitHub benchmark repositories (mentioned in the experiment section), as well as additional milestone or state-of-the-art approaches. Many of these methods also overlap with those covered in previous review papers. However, most of these reviews primarily focus on radiology images, overlooking the unique characteristics of pathology images, such as their scale, large image sizes, and repetitive patterns.

Compared to previous work, our contributions are as follows: 1) Reviewing anomaly detection methods specifically applied to pathology images. 2) Summarizing the domain-specific characteristics of pathology image anomaly detection, and introducing real and synthetic datasets tailored for analysis. 3) Exploring a practical yet challenging problem—unbiased training epoch selection—which has not been systematically examined in prior work. 4) Applying representative benchmark methods to pathology image anomaly classification tasks, providing empirical insights into their performance in this domain.

III. ANOMALY DETECTION ALGORITHM

A. Anomaly detection in vision domain

The strict anomaly detection algorithm we discuss here can only access normal data during the training phase, which is denoted as $D_{\text{train}} = \{X_{\text{normal}}\}$. The goal of an anomaly detection algorithm is to learn a function $\alpha(x, \theta)$ that distinguishes X_{normal} from X_{abnormal} . Typically, a projection head Φ is also introduced to convert the result of $\alpha(x, \theta)$ into a numeric result, known as the anomaly score. This anomaly score is used to classify X_{normal} and X_{abnormal} in the test set. Generally, it holds that $\Phi(\alpha(x_{\text{normal}}, \theta)) < \Phi(\alpha(x_{\text{abnormal}}, \theta))$.

Since the training set does not include abnormal data, the core idea of the algorithm is to learn the **feature distribution of normal data** or the **behavior of some tasks (e.g., reconstruction, denoising) on normal data**. The feature distribution of unseen abnormal data or its behavior in a specific task is expected to differ from that of normal data, thereby enabling classification during the inference phase.

The reviewed anomaly detection algorithms are mentioned and categorized into different types, as shown in Fig. 2, including reconstruction-based method, feature distribution method, distillation method, synthetic abnormality and normalizing flow method. The characteristics of these methods are summarized in Table I.

TABLE I
SUMMARY OF ANOMALY DETECTION METHODS CATEGORIZED BY TYPE, WITH THEIR MAIN IDEAS, TECHNIQUES, ADVANTAGES, LIMITATIONS, AND REPRESENTATIVE WORKS.

Method Type	Main Idea	Techniques	Advantages	Limitations	Representative Work
Image Reconstruction	Train models to reconstruct normal images and use reconstruction errors to identify anomalies.	AE/VAE, GAN, Diffusion models	Offers visual interpretability through reconstruction error maps.	May reconstruct abnormal data well; sensitive to model architecture (e.g., bottleneck size).	UniAD [11], [12], IGD [13], [14], AMCons [15], GANomaly [16], FAE [17], DFR [18], HATES [19]
Feature Distribution	Model the distribution of feature embeddings extracted from normal data; anomalies deviate from this distribution.	Memory Bank, One-Class SVM, KNN, Clustering, GMM	Works well with high-dimensional data; flexible integration with pre-trained models.	Sensitive to noise and sparsity in embeddings; requires meaningful features.	PANDA [20], PatchCore [21], CFA [22], DFKDE [23], [24], PaDiM [25]
Distillation	Use knowledge distillation to train a compact model to mimic a teacher model; discrepancies are treated as anomalies.	Knowledge distillation, Feature alignment	Efficient inference with smaller model size.	Performance depends on teacher quality and distillation design.	Reverse Distillation [26], Revisit Distillation [27], STFPM [28], ReContrast [29]
Normalizing Flow	Learn exact data distributions using invertible transformations; use likelihood scores for anomaly detection.	Flow-based likelihood estimation	Expressive modeling of complex distributions.	Computationally expensive, especially on large-scale data.	FastFlow [30], CFLOW-AD [31], CS-Flow [32]
Synthetic Anomaly Detection	Introduce synthetic anomalies during training; train the model to distinguish them from normal data.	Self-supervised learning, Data augmentation	Adaptable to various anomaly types through creative augmentations.	Effectiveness depends on the quality/diversity of synthetic anomalies.	CutPaste [33], DRAEM [12]

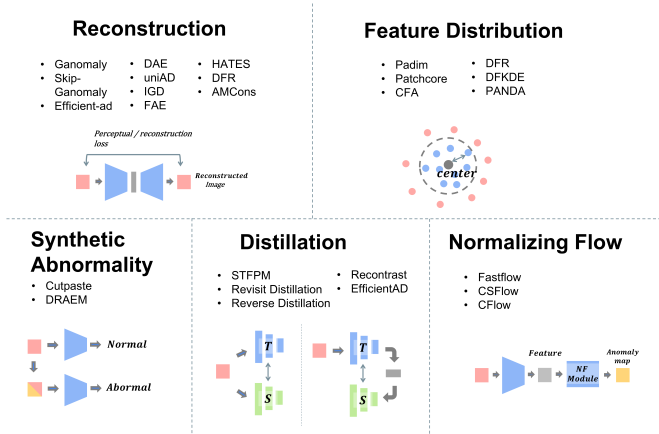


Fig. 2. **Classification of anomaly detection models across five methodological families: reconstruction-based, feature distribution-based, distillation-based, normalizing flow-based, and synthetic anomaly-based methods.** Each family represents a distinct algorithmic principle for distinguishing anomalies from normal data. Reconstruction-based methods rely on detecting pixel-level differences, feature distribution methods model the latent space of normality, distillation methods leverage teacher–student discrepancies, normalizing flows model exact likelihood distributions, and synthetic approaches train models on augmented anomalies. These groupings are important as they highlight varying strengths and limitations when applied to the complex structure of pathology images.

Reconstruction-based methods aim to reconstruct input images and flag discrepancies as anomalies based on reconstruction errors. Simpler architectures, such as autoencoders (AE/VAE), compress and reconstruct images. For example, IGD [13] proposes fusing latent features within a Gaussian-distributed latent space to learn a smoother and more representative normal space. The HATES [19] uses transformer

blocks for autoencoder-based reconstruction, while FAE [17] adopts the Structural Similarity Index Measure (SSIM) as an optimization objective. However, the bottleneck structure in autoencoders limits the expressiveness of abnormal patterns and simultaneously discards normal pattern information, leading to blurry reconstructions. Increasing the bottleneck size may help retain more information but risks also reconstructing anomalous content. To address this, DAE [14] introduces denoising strategies to recover meaningful signals and mitigate over-compression. Similarly, UniAD [11] employs a feature jittering strategy to encourage the model to recover the correct representation from noisy inputs. In addition, generative adversarial networks (GANs), such as GANomaly, and diffusion-based methods, such as AnoDDPM, have been introduced to produce higher-quality reconstructions with clearer details.

Feature distribution-based methods operate in the latent feature space by modeling the distribution of embeddings extracted from normal data. Techniques such as PatchCore, PANDA, PaDiM, and DFKDE rely on pretrained backbone networks to estimate feature statistics. These methods are typically more robust to complex patterns, as they do not depend on pixel-level reconstruction fidelity. PaDiM [25] and DFKDE [23] extract features using pretrained models and model them with multivariate Gaussian distributions. PatchCore [21] constructs a memory bank via core-set sampling and uses nearest neighbor voting to classify predictions as normal or abnormal. CFA [22] enhances the Patchcore by organizing image features on a hyperspherical feature space. PANDA learns a compact feature space representing normal patterns, with anomalies expected to fall outside this learned manifold.

Knowledge distillation-based methods adopt a

teacher–student paradigm, where the student network learns to replicate the outputs or feature representations of a teacher network on normal data. A significant discrepancy between the student and teacher on abnormal samples indicates potential anomalies. Representative approaches include STFPM [28], reverse distillation [26], ReContrast [29], and revisit distillation [27].

Normalizing flow-based methods model the likelihood of normal data through invertible transformations. These methods offer principled probabilistic anomaly scoring based on exact density estimation. However, they are often limited by high computational cost and sensitivity to architectural choices. CFLOW-AD [31] incorporates positional encoding alongside flow-based modules, while CS-Flow [32] integrates multi-scale features for more accurate distribution estimation.

Finally, synthetic anomaly-based methods, such as Cut-Paste [33] and DRAEM [12], simulate artificial anomalies through data augmentation or generative modeling. These methods enable training without real anomaly labels by teaching the model to distinguish between original and perturbed samples. For instance, CutPaste trains two separate encoders using a three-way classification task, distinguishing each input image from two variants with synthetic anomalies—designed for both image-level detection and pixel-level localization. The effectiveness of these methods heavily depends on the diversity and realism of the synthetic patterns, which may not always reflect true clinical abnormalities.

The methods outlined above represent the major families of anomaly detection techniques in the computer vision literature. In the following section, we review how anomaly detection methods have been adapted and applied to pathology images. In our study, we selected 23 representative algorithms spanning these five categories to systematically benchmark their performance in the domain of digital pathology.

B. Anomaly detection in pathology images

With the development of anomaly detection algorithms in the field of natural images, some studies have extended these algorithms to pathology images. Most of these approaches were based on reconstruction-based techniques. For instance, recent studies [34]–[36] have utilized autoencoders to reconstruct normal images under the assumption that anomalies, unseen during training, will produce higher reconstruction errors. However, pixel-wise reconstruction scores can be overly sensitive to local artifacts such as edges or background regions, and may fail to capture meaningful global semantic discrepancies. To address this, perceptual loss [37] is often incorporated as an auxiliary loss and anomaly scoring metric in these autoencoder-based methods. Despite this improvement, autoencoder-reconstructed images often remain blurry. To generate higher-quality reconstructions, Generative Adversarial Network (GAN)-based and diffusion-based methods have been introduced. GANomaly [38] pioneered the application of GANs to anomaly detection, and [39] adapted this framework to pathology images. Similarly, [36] and [5] utilized StyleGAN as the generative backbone, while [3] leveraged Progressive

GAN for producing high-resolution pathology images. More recently, [40] employed the diffusion-based AnoDDPM model for pathology image reconstruction.

Feature distribution-based anomaly detection typically leverages the strong representational power of pre-trained models to distinguish between normal and abnormal images. Although its application in medical imaging, especially in the domain of pathology images, is less common than reconstruction-based approaches, it has demonstrated promising performance in several prior studies. For example, [4] employed a pre-trained model and an auxiliary classification task to train a classification backbone for extracting image features. They used central loss to learn a compact representation of normal features, which helps distinguish the dispersed distribution of abnormal features.

It is especially worth noting that many anomaly detection algorithms have undergone adaptations to better suit the complex nature of pathology images. For example, Gu et al. [3] and Shvetsova et al. [34] adopted progressive training strategies to capture the fine details of pathology images. [35] introduced skip connections similar to U-Net architectures to retain more details. To further align feature extraction with pathology images, Zingman et al. [4] defined an auxiliary classification task of normal mouse liver tissue, which is the same image domain for anomaly detection. This approach makes pre-trained models on ImageNet more suitable for extracting features from mouse liver images. Considering stain variations of pathology images, this study also proposed using mix-up color augmentation to reduce color sensitivity while preserving sensitivity to structural differences. Additionally, Lai et al. [39] simulated anomalies such as enlarged cell nuclei or irregular tissue structures when adapting CutPaste and local magnification techniques during training. The scale of pathology images is another important factor. Both Lat et al. [39] and Shvetsova et al. [34] considered the impact of scale and extracted multi-scale features to improve anomaly detection performance.

As for anomaly score calculation, in addition to common metrics such as Mean Squared Error (MSE), other similarity measures like learned perceptual image patch similarity (LPIPS) and structural similarity index measure (SSIM), as well as perceptual loss, are used to evaluate the similarity between generated and original images. Different metrics may show consistency or complement each other. Many studies combine multiple metrics for anomaly score computation, but the choice and weighting of these metrics need to be adjusted based on specific applications.

Since whole-slide images (WSIs) in pathology are too large to process directly, they are typically divided into patches. Anomaly scores are computed for each patch, and the WSI-level result is obtained by averaging or taking the maximum score. The choice of aggregation strategy can also affect the results. [4] discussed other aggregation strategies that can be considered.

However, these studies only used a fixed number of training epochs and did not further discuss how to fine-tune this

TABLE II
DATASETS AND THE CORRESPONDING DATA SPLITS USED IN THIS WORK

Dataset	Scale	Training	Validation		Testing	
		Normal	Normal	Abnormal	Normal	Abnormal
Synthetic Dataset	small scale	1536	1024	1024	1024	1024
	large scale	24	16	16	16	16
Colon	small scale	3408	1136	1264	1280	1280
	large scale	213	71	79	80	80
Glomerulus	small scale	649	71	71	69	65
	large scale	649	71	71	69	65
Camelyon	combined	5462	2150	2169	4000	817
Hazelnut	combined	391	9	12	31	58
Tile	combined	201	29	19	33	65

important parameter, especially when the validation set may also lack abnormal images. Our subsequent experiments focus on this often-overlooked issue. In addition, we conducted a more detailed analysis of the impact of multiscale features on anomaly detection in pathology images using both real and synthetic datasets.

IV. DATA AND EXPERIMENTS

A. Data

The dataset characteristics are summarized in Table II. This study uses three real-world pathology image datasets, two synthetic datasets, and two industrial defect datasets to evaluate different anomaly detection algorithms. Each dataset is divided into training, validation, and testing sets. The training set contains only normal data, while the testing set includes both normal and abnormal data, sharing a similar distribution to the validation set. Examples of normal and abnormal images are provided in Fig. 3.

1) *Pathology Images: Breast Pathology Dataset [41]*. Detecting lymph node metastases is a key factor in breast cancer diagnosis. The Camelyon16 challenge [42] offers a public dataset for metastasis detection in digital pathology. Its training set includes 110 tumor-positive and 160 normal H&E stained whole slide images (WSIs), while the test set contains 50 tumor-positive and 80 normal WSIs, with pixel-level tumor annotations. Following prior work [34], we preprocess the 40×magnification WSI data into 768×768 patches for training, validation, and testing. Tumor patches are extracted from annotated tumor regions, while normal patches come from non-tumor regions. We used the same test set as previous work, consisting of 4000 normal and 817 abnormal patches. For validation, we randomly selected 2169 tumor and 2150 normal patches from the WSIs in the Camelyon16 training set, leaving 5462 normal patches for training. In contrast, previous work used all 7612 normal patches across our training and validation for model training.

Colon Pathology Dataset [43]. Biopsies of 16 Crohn’s disease (CD) patients and 53 healthy controls collected from the colon. The tissues were stained with H&E and scanned at 20×magnification. Large patches in size 1812 × 1812 were cropped from the WSIs and labeled by pathologists as either normal or abnormal (diseased). To explore the impact of different scales on anomaly detection, we further tiled the large patches into smaller patches of 512 × 512. Predictions on the small patches are aggregated and compared with predictions

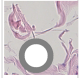
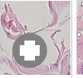
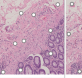
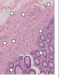
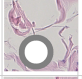
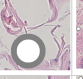
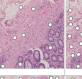
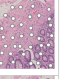
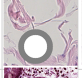
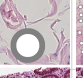
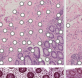
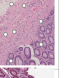
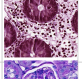
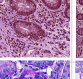
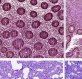
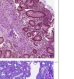
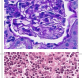
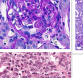
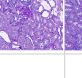

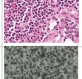
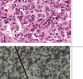


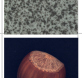
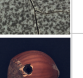
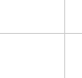


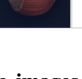


Type	Name	Magnification	Patch Scale	Normal	Abnormal	Normal	Abnormal
				Small Scale		Large Scale	
Synthetic Data	Circle /Cross	20x	2048 x 2048 /256 x 256				
	Low/High Density	20x	2048 x 2048 /256 x 256				
	Low/High Density - Reverse	20x	2048 x 2048 /256 x 256				
Pathology Images	Colon	20x	1812 x 1812 /512 x 512				
	Glomerulus	20x	3072 x 3072 /512 x 512				
	Camelyon	40x	768 x 768				
Industry Device	Tile	N/A	256				
	Hazelnut	N/A	256				

Fig. 3. **Overview of the datasets and example images spanning diverse digital pathology and industrial imaging modalities.** The datasets include real-world pathology images (e.g., colon, glomerulus, Camelyon), synthetic pathology images with designed patterns, and standard industrial datasets (e.g., Hazelnut, Tile). This breadth ensures comprehensive evaluation across different anomaly types, image scales, and domain complexities, providing robust insights into the generalizability of each detection method.

from the large patches to evaluate the performance across scale.

Kidney Pathology Dataset [44]. This dataset consists of both benign and malignant glomeruli of mice. We extracted center-cropped patches with benign or malignant glomeruli at sizes of 3072 × 3072 and 512 × 512 separately from the WSIs stained by H&E at 40× magnification. Normal patches are retained only if all glomeruli within them are normal.

2) *Synthetic Images*: Investigating abnormal patterns in pathology images presents significant challenges due to their complexity. So, we incorporated synthetic datasets to analyze model performance in a controlled environment. By utilizing 56 patches in 2048 × 2048 pixels tiled from 20× normal WSIs in the Unitopatho dataset [45], we overlay synthetic patterns designed specifically for anomaly detection. This approach enables the simulation of various scenarios pertinent to digital pathology.

Circle or Cross Patterns. To synthesize the morphological difference of normal and abnormal tissue, we introduced gray circles with a radius of 60 pixels on 2048 × 2048 patches and designed two distinct patterns: one consisting of white circles positioned within the gray circles, and the other featuring white crosses instead of circles.

To assess the impact of different magnification levels, we prepared two scales of abnormality. At the 20× magnification

(large scale), we resized the 2048×2048 patches to 256×256 for analysis. For the small-scale patches, we tiled the above 2048×2048 patches into small patches of size 256×256 . The prediction results from the small scale will be aggregated and compared with those from the large scale. Distinguishing between the circle and cross patterns is relatively straightforward on the small scale, while it presents greater difficulty on the large scale.

Density Patterns. Cell density is another critical component in anomaly detection in digital pathology images. We continued to use the concentric circles mentioned previously as the primary element but modified their density within the 2048×2048 patches. In this setup, we divided the patches into 256×256 grids and assigned probabilities for each grid containing a circle, with one pattern reflecting a 75% probability and another reflecting a 25% probability.

Similar to the previous experiment, we prepared two scales of patches for this dataset. Theoretically, the large-scale observations should facilitate easier detection of density differences compared to those observed at the small scale.

3) *Industrial Device Images:* We also incorporated two classes of industrial defect anomaly detection datasets [46], which are commonly used benchmarks in the natural image domain. Specifically, we utilized the **Hazelnut dataset** to represent object abnormalities and the **Tile dataset** to capture texture abnormalities. These datasets serve as benchmarks, allowing us to illustrate the gap between the anomaly detection of industrial device images and medical images. As a validation set is not available in this dataset, we extracted a small portion of the testing data as the validation set in our experiment.

B. Experiment Settings

In our experiments, the validation set is prepared in two configurations: a complete version with both normal and abnormal data, and a strict, unbiased version with only normal data. We analyze and compare different model selection strategy under these two validation setups in our experiments. Additionally, as detailed further in this section, we explore the impact of different pathology image scales and the reversion of abnormal patterns on model performance. Anomaly detection algorithms are applied to the prepared datasets described above, with three sets of experiments conducted for analysis.

1) *Impact of Different Scales:* For the in-house colon dataset, in-house glomerulus dataset, and the synthetic datasets, we do anomaly detection in different scales. The patches in a smaller scale were tiled from the same region in the original WSIs and contained more detail than the larger scale. The integration of the small region is used as the final prediction results to compare with the prediction of the larger scale.

2) *Unbiased Training Epoch Selection:* An important yet often overlooked challenge in anomaly detection is selecting the appropriate training epoch for the model. In most cases, only normal data is available during the training phase, leaving no complete validation set to determine the optimal epoch

as in supervised training. Even when limited abnormal data are available, they may lack the diversity and generality needed to represent all possible abnormal scenarios, potentially introducing bias. Furthermore, stopping the training process at different epochs can lead to significantly different outcomes, yet previous research has not sufficiently addressed the criteria for selecting training epochs. Following the work of [47], we implement four training epoch selection methods, including both with and without the inclusion of abnormal data during the training phase, to facilitate a broader comparison. Specifically, these four methods are:

- **Strategy 1 - Normal Sample Loss Evaluation:** This method, proposed by [20], involves saving multiple model checkpoints from different epochs during training. During the testing phase, the anomaly score for each sample is calculated at various checkpoints and normalized by the corresponding average anomaly score of normal samples in the validation set, resulting in a value known as the maximal ratio. The checkpoint with the highest ratio indicates the best separation for that testing sample, and this maximal ratio serves as the anomaly score for the sample. The rationale behind this approach is that the maximum deviation ratio of a sample during the testing phase, compared to normal data in the validation set, reflects how likely the sample is to be abnormal. With this method, the number of epochs used to calculate the anomaly score may vary across different samples.
- **Strategy 2 - Complete Validation Set Method:** This method utilizes a complete validation set containing both normal and abnormal data. The epoch with the highest Area Under the Curve (ROC-AUC) score on this validation set is selected. If the data distribution of the validation set closely resembles that of the testing set, this method can serve as the upper bound for model selection performance as supervised learning.
- **Strategy 3 - Normal Sample Loss Evaluation:** This strategy evaluates the loss of normal samples in the validation set to determine how effectively the model has been trained on the pretext task, such as image reconstruction. The point of minimal loss indicates the best-trained model, which is then used for testing.
- **Strategy 4 - Last Epoch Selection:** This strategy assumes that training has either converged or the model has overfitted to the training samples. In this case, the model from the final epoch is directly selected for testing. As highlighted in [20], continual learning can help ensure stable training, making the last epoch a reasonable choice.

3) *Reversion of the normality and abnormality:* The difficulty of learning diverse normal patterns can vary significantly. To investigate this, we reversed the definitions of normal and abnormal in the synthetic density dataset by swapping the normal and anomaly patterns. We then repeated the experiments to analyze the impact of this reversal.

The implementations of CS-Flow [32], CFA [22], DFM [24], DFKDE [23], DRAEM [12], EfficientAD [23],

FastFlow [30], GANomaly [38], PADIM [25], PatchCore [21], and STFPM [28] were sourced from the GitHub repository: <https://github.com/openvinotoolkit/anomalib>. Similarly, CFLOW-AD, DAE [14], DFR [18], FAE [17], HATES [19], and Reverse Distillation were obtained from another repository: https://github.com/iolag/UPD_study. The remaining algorithms—SkipGanomaly [48], Revisit Distillation, PANDA [20], IGD [13], ReContrast [29], and UniAD [11]—were implemented using code from their respective official GitHub repositories.

For a fair comparison, we standardized the experimental setup as follows: input image sizes were unified to 256×256 , with 200 training epochs and a batch size of 16. Pretrained weights were loaded when available, and images were standardized using the default mean and standard deviation values for ImageNet. Data augmentation included horizontal flipping, while most of the original parameters were retained.

For anomaly detection algorithms, a single anomaly score was obtained for each patch. When aggregation was required for object-wise or patient-wise results, the average of the top 20% highest anomaly scores was used as the final anomaly score. A higher anomaly score indicates a greater likelihood of abnormality. The ROC-AUC metric was employed to evaluate the performance of the anomaly detection algorithms. Here is a refined version:

A higher ROC-AUC indicates better separation and effectiveness of the method in detecting anomalies.

All experiments were conducted using an NVIDIA RTX 4090 GPU.

V. RESULTS AND DISCUSSION

A. Results Analysis

Results of experiments are shown in Table III and IV.

1) *General Comparison among Different Methods and Datasets*: There is no method that performs consistently the best among all datasets. This discovery also aligns with the conclusion in prior work [47]. Meanwhile, some methods achieve competitive performance in some datasets (obviously above average) but almost fail (obviously below the average) in other datasets, for example Reverse distillation, skipGanomaly and uniAD, etc. Overall, feature distribution-based anomaly detection methods outperform both distillation-based and reconstruction-based approaches, achieving higher object-level ROC-AUC averages when using the complete validation set for epoch selection (distribution-based approaches: 0.692, distillation-based: 0.600, reconstruction-based approaches: 0.564). This trend is especially notable for pathology-type images and has also been observed in [9]. Reconstruction-based methods are often limited by the unpredictable generalization. Sometimes anomalous images are reconstructed well, while some normal images are rendered overly blurry. Given the abundance of fine-grained patterns in pathology images, feature-based anomaly detection is often more robust than pixel-based error or variance metrics. Unlike distillation-based methods, which compress

features through a teacher–student framework, distribution-based approaches model the feature space extracted from normal images directly. These methods typically preserve richer detail in the original feature space, making them more sensitive to subtle or unstructured anomaly patterns. Also, the average ROC-AUC for industrial device datasets is significantly higher than that for synthetic datasets and much higher than for real pathology datasets. This highlights the complexity and challenges associated with pathology images, particularly real pathology images. Methods that perform well on industrial datasets may not be sufficient to effectively distinguish between normal and abnormal cases in digital pathology images.

2) *Impact of Different Scales*: For synthetic data, as expected, smaller scales perform better for anomaly patterns like crossing and circles because the details are more distinct in smaller patches. In contrast, for density-related abnormalities, larger scales, which capture global information, outperform smaller scales that lack sufficient context to reflect density changes. In the case of the Glomerulus dataset, which has patterns similar to synthetic data with crossing and circles, smaller scales also perform better (avg ROC-AUC of small scale: 0.650, avg scale of large scale: 0.611). However, for the colon dataset, larger scales yield superior performance (avg ROC-AUC of large scale: 0.767, avg scale of small scale: 0.640). These findings underscore the critical role of scale in anomaly detection. While many methods, such as distillation, PANDA, and PADIM, leverage features from different network layers to capture multi-scale information, these approaches are insufficient when compared to the significant scale differences present in pathology images.

3) *Unbiased Training Epoch Selection*: Regarding training epoch selection strategies, the method using the complete validation set consistently achieves the best performance with the highest average ROC-AUC for all three kinds of datasets. The sample-wise strategy ranks second, followed by the loss-based method in third place. The last-epoch method, while the simplest, performs the worst on average. 20 datasets, last epoch selection consistently performs the worst (19 out of 20), and the best and second-best performances are achieved by val and sample-wise respectively in 15 out of 20 datasets. Both the sample-wise and loss-based strategies are unbiased since they do not require abnormal samples. The sample-wise strategy performs slightly better in our experiments, but it demands more memory to save models at various checkpoints and requires additional computation time.

We also report PR-AUC values in Table IV, which show a similar overall trend to ROC-AUC. Training epochs selected based on the full validation set generally achieved the highest PR-AUC, while the loss-based selection method also performed well and yielded results comparable to the sample-wise strategy.

PR-AUC ignores true negatives and focuses more on the precision and recall of the positive class. It is more suitable for imbalanced datasets where the positive class is rare and false positives are costly. However, except for the Camelyon, Hazelnet, and Tile datasets, the test sets in our study are

TABLE III

EXPERIMENT RESULTS (ROC-AUC): THIS TABLE PRESENTS THE PERFORMANCE OF VARIOUS ANOMALY DETECTION METHODS UNDER DIFFERENT EPOCH SELECTION STRATEGIES ACROSS MULTIPLE DATASETS. THE FOUR STRATEGIES INCLUDE: SAMPLE-WISE BEST EPOCH SELECTION (SAMPLE), BEST EPOCH BASED ON THE FULL VALIDATION SET (VAL), EPOCH WITH THE MINIMUM TRAINING LOSS (LOSS), AND THE FINAL EPOCH (LAST). THE RESULT HIGHLIGHTED IN RED INDICATES THE HIGHEST ROC-AUC AMONG ALL STRATEGIES, WHILE BLUE DENOTES THE SECOND-HIGHEST. KEY OBSERVATIONS: 1) OVERALL, FEATURE DISTRIBUTION-BASED ANOMALY DETECTION METHODS OUTPERFORM BOTH DISTILLATION-BASED AND RECONSTRUCTION-BASED APPROACHES. 2) BASED ON THE AVERAGE RESULTS FOR SAMPLE-WISE SELECTION ACROSS 20 DATASETS, LAST EPOCH SELECTION CONSISTENTLY PERFORMS THE WORST (19 OUT OF 20), AND THE BEST AND SECOND-BEST PERFORMANCES ARE ACHIEVED BY VAL AND SAMPLE-WISE RESPECTIVELY IN 15 OUT OF 20 DATASETS. OVERALL, THE RANKING IS: VAL > SAMPLE-WISE > LOSS > LAST. 3) IMAGE SCALE SIGNIFICANTLY AFFECTS DETECTION PERFORMANCE. DESPITE MANY METHODS INCORPORATING MULTI-SCALE INFORMATION, DIRECTLY USING IMAGE PATCHES OF DIFFERENT SCALES STILL LEADS TO NOTABLE DIFFERENCES IN RESULTS, ESPECIALLY IMPORTANT IN PATHOLOGY IMAGES WHERE SCALE VARIATION IS LARGE. 4) ON SYNTHETIC DENSITY DATASETS, REVERSING THE DEFINITIONS OF NORMAL AND ABNORMAL YIELDS DIFFERENT RESULTS. THIS SUGGESTS THAT THE DIFFICULTY OF MODELING NORMAL PATTERNS ALSO IMPACTS ANOMALY DETECTION PERFORMANCE.

	Synthetic Pathology Image Datasets																											
Dataset	Normal - circle / Abnormal - crossing								Normal - high density / Abnormal - low density								Normal - low density / Abnormal - high density								Average			
Scale	2048				256				2048				256				2048				256							
Best epoch	Sample	Val	Loss	Last	Sample	Val	Loss	Last	Sample	Val	Loss	Last	Sample	Val	Loss	Last	Sample	Val	Loss	Last	Sample	Val	Loss	Last	Sample	Val	Loss	Last
DFM	0.477	0.477	0.477	0.477	0.695	0.695	0.695	0.695	0.996	0.996	0.996	0.996	0.656	0.656	0.656	0.656	0.613	0.613	0.613	0.613	0.480	0.480	0.480	0.480	0.653	0.653	0.653	0.653
DFKDE	0.582	0.582	0.582	0.582	0.559	0.559	0.559	0.559	0.996	0.996	0.996	0.996	0.785	0.785	0.785	0.785	0.820	0.820	0.820	0.820	0.258	0.258	0.258	0.258	0.667	0.667	0.667	0.667
PaDiM	0.605	0.605	0.605	0.605	1.000	1.000	1.000	1.000	0.949	0.949	0.949	0.949	0.523	0.523	0.523	0.523	0.953	0.953	0.953	0.953	0.559	0.559	0.559	0.559	0.765	0.765	0.765	0.765
Patchcore	0.570	0.570	0.570	0.570	1.000	1.000	1.000	1.000	0.836	0.836	0.836	0.836	0.461	0.461	0.461	0.461	0.516	0.516	0.516	0.516	0.527	0.527	0.527	0.527	0.652	0.652	0.652	0.652
Revisit Distillation	0.574	0.602	0.508	0.508	1.000	1.000	1.000	1.000	0.895	0.957	0.945	0.945	0.660	0.652	0.609	0.633	0.473	0.859	0.281	0.281	0.945	0.969	0.422	0.426	0.758	0.840	0.628	0.632
PANDA	0.586	0.582	0.605	0.594	0.703	0.828	0.711	0.701	0.980	0.988	0.957	0.977	0.719	0.754	0.758	0.762	0.906	0.914	0.891	0.895	0.414	0.422	0.383	0.371	0.718	0.748	0.717	0.716
IGD	0.648	0.668	0.590	0.633	0.846	0.941	0.664	0.727	0.914	0.934	0.938	0.934	0.715	0.773	0.750	0.758	0.902	0.934	0.934	0.922	0.477	0.625	0.469	0.461	0.750	0.813	0.724	0.739
ReContrast	0.473	0.602	0.531	0.324	1.000	1.000	1.000	1.000	0.871	0.848	0.895	0.895	0.555	0.664	0.527	0.527	0.434	0.480	0.461	0.461	0.563	0.813	0.293	0.293	0.648	0.734	0.618	0.583
UniAD	0.363	0.395	0.340	0.324	0.555	0.586	0.510	0.512	0.953	0.973	0.941	0.926	0.504	0.570	0.508	0.508	0.199	0.328	0.039	0.039	0.512	0.527	0.488	0.488	0.514	0.563	0.471	0.466
CS-FLOW	0.723	0.719	0.766	0.656	0.949	0.988	0.840	0.445	0.800	0.750	0.800	0.887	0.688	0.652	0.387	0.430	0.492	0.492	0.375	0.406	0.441	0.633	0.598	0.340	0.682	0.706	0.628	0.527
CFA	0.520	0.547	0.523	0.492	1.000	1.000	0.566	0.395	0.676	0.742	0.730	0.730	0.961	1.000	0.488	0.523	0.648	0.691	0.578	0.578	0.527	0.527	0.520	0.418	0.722	0.751	0.568	0.523
DRAEM	0.766	0.922	0.680	0.875	1.000	1.000	1.000	1.000	0.688	0.734	0.762	0.645	0.586	0.633	0.539	0.609	0.594	0.680	0.477	0.645	0.922	1.000	0.551	0.656	0.759	0.828	0.668	0.738
EfficientAD	0.461	0.723	0.391	0.445	0.625	0.797	0.820	0.730	0.520	0.629	0.473	0.488	0.543	0.504	0.590	0.547	0.461	0.563	0.363	0.367	0.465	0.406	0.484	0.461	0.512	0.604	0.520	0.507
FastFlow	0.734	0.688	0.723	0.773	1.000	1.000	0.977	0.434	1.000	1.000	1.000	1.000	1.000	1.000	1.000	1.000	0.030	0.031	0.023	0.008	0.750	0.961	0.430	0.840	0.752	0.780	0.692	0.676
GANomaly	0.402	0.461	0.594	0.480	0.582	0.598	0.449	0.598	0.633	0.617	0.512	0.500	0.531	0.504	0.539	0.449	0.348	0.414	0.582	0.500	0.496	0.574	0.539	0.574	0.499	0.528	0.536	0.517
STFPM	0.500	0.527	0.586	0.555	0.957	1.000	0.941	1.000	0.938	0.926	0.875	0.895	0.082	0.512	0.055	0.008	0.105	0.477	0.242	0.262	0.426	0.465	0.453	0.508	0.501	0.651	0.525	0.538
CFLOW-AD	0.520	0.555	0.527	0.527	1.000	1.000	1.000	1.000	0.664	0.605	0.652	0.813	0.609	0.664	0.672	0.621	0.684	0.508	0.637	0.410	0.633	0.668	0.543	0.551	0.685	0.667	0.672	0.654
DAE	0.527	0.656	0.598	0.516	0.520	0.551	0.531	0.521	0.797	0.887	0.500	0.492	0.623	0.531	0.512	0.547	0.301	0.609	0.582	0.473	0.516	0.539	0.484	0.477	0.531	0.629	0.535	0.504
DFR	0.406	0.469	0.469	0.488	1.000	1.000	1.000	1.000	0.621	0.688	0.664	0.664	0.457	0.480	0.469	0.473	0.719	0.730	0.668	0.621	0.820	0.914	0.621	0.621	0.671	0.714	0.648	0.645
FAE	0.434	0.473	0.465	0.469	0.518	0.523	0.480	0.477	1.000	1.000	0.988	0.996	0.695	0.691	0.715	0.715	0.547	0.715	0.375	0.488	0.391	0.473	0.277	0.254	0.597	0.646	0.550	0.566
HTAES	0.313	0.543	0.180	0.238	0.602	0.961	0.547	0.777	0.484	0.449	0.492	0.395	0.605	0.699	0.578	0.629	0.555	0.813	0.699	0.645	0.691	0.965	0.441	0.457	0.542	0.738	0.490	0.523
Reverse Distillation	0.477	0.473	0.477	0.469	1.000	1.000	1.000	1.000	0.785	0.789	0.711	0.570	0.648	0.676	0.695	0.711	0.457	0.414	0.379	0.367	0.418	0.438	0.352	0.387	0.631	0.632	0.602	0.584
SkipGanomaly	0.414	0.430	0.402	0.402	0.738	1.000	0.533	0.469	0.352	0.352	0.352	0.352	0.457	0.484	0.457	0.453	0.648	0.648	0.648	0.648	0.508	0.516	0.516	0.504	0.520	0.672	0.485	0.471
Average by epoch selection method	0.525	0.577	0.530	0.522	0.819	0.871	0.775	0.741	0.798	0.811	0.781	0.777	0.607	0.647	0.577	0.579	0.539	0.618	0.528	0.518	0.554	0.620	0.465	0.474	0.640	0.690	0.609	0.602
Average by dataset	0.538				0.802				0.792				0.603				0.551				0.528				0.636			

Dataset	Industrial Device Datasets																Real Pathology Images Datasets																																																							
	Hazelnut								Average								Glomerulus								2048								Cameleon								2048								Colon								512								Average							
	Sample	Val	Loss	Last	Sample	Val	Loss	Last	Sample	Val	Loss	Last	Sample	Val	Loss	Last	Sample	Val	Loss	Last	Sample	Val	Loss	Last	Sample	Val	Loss	Last	Sample	Val	Loss	Last	Sample	Val	Loss	Last	Sample	Val	Loss	Last																																
Best epoch	Sample	Val	Loss	Last	Sample	Val	Loss	Last	Sample	Val	Loss	Last	Sample	Val	Loss	Last	Sample	Val	Loss	Last	Sample	Val	Loss	Last	Sample	Val	Loss	Last	Sample	Val	Loss	Last	Sample	Val	Loss	Last	Sample	Val	Loss	Last																																
DFM	0.982	0.982	0.982	0.982	0.985	0.985	0.985	0.985	0.983	0.983	0.983	0.983	0.876	0.876	0.876	0.876	0.712	0.712	0.712	0.712	0.515	0.515	0.515	0.515	0.995	0.995	0.995	0.995	0.809	0.809	0.809	0.809	0.781	0.781	0.781	0.781																																				
DFKDE	0.792	0.792	0.792	0.792	0.939	0.939	0.939	0.939	0.866	0.866	0.866	0.866	0.774	0.774	0.774	0.774	0.560	0.560	0.560	0.560	0.807	0.807	0.807	0.807	0.860	0.860	0.860	0.860	0.894	0.894	0.894	0.894	0.779	0.779	0.779	0.779																																				
PaDiM	0.731	0.731	0.731	0.731	0.959	0.959	0.959	0.959	0.845	0.845	0.845	0.845	0.763	0.763	0.763	0.763	0.544	0.544	0.544	0.544	0.381	0.381	0.381	0.381	0.723	0.723	0.723	0.723	0.665	0.665	0.665	0.665	0.615	0.615	0.615	0.615																																				
Patchcore	0.870	0.870	0.870	0.870	0.827	0.827	0.827	0.827	0.849	0.849	0.849	0.849	0.786	0.786	0.786	0.786	0.649	0.649	0.649	0.649	0.558	0.558	0.558	0.558	0.956	0.956	0.956	0.956	0.833	0.833	0.833	0.833	0.756	0.756	0.756	0.756																																				
Revisit Distillation	1.000	0.951	1.000	1.000	0.982	0.986	0.983	0.986	0.991	0.969	0.992	0.993	0.616	0.596	0.647	0.655	0.536	0.597	0.716	0.704	0.722	0.735	0.619	0.614	0.913	0.926	0.909	0.929	0.425	0.668	0.614	0.614	0.642	0.704	0.741	0.743																																				
PANDA	0.957	0.975	0.963	0.963	0.990	0.996	0.996	0.996	0.973	0.981	0.974	0.971	0.882	0.885	0.885	0.885	0.610	0.663	0.664	0.647	0.938	0.943	0.944	0.944	0.987	0.990	0.983	0.983	0.911	0.930	0.879	0.879	0.866	0.862	0.871	0.868																																				
IGD	0.945	0.945	0.943	0.955	0.974	0.975	0.971	0.966	0.982	0.980	0.957	0.960	0.730	0.787	0.685	0.695	0.620	0.543	0.541	0.668	0.927	0.827	0.465	0.348	0.983	0.998	0.998	0.998	0.682	0.856	0.550	0.544	0.788	0.822	0.649	0.648																																				
ReContrast	1.000	0.997	1.000	1.000	0.998	0.995	0.997	0.998	0.999	0.998	0.999	0.999	0.709	0.816	0.695	0.626	0.627	0.792	0.743	0.729	0.691	0.851	0.467	0.467	0.926	0.932	0.917	0.917	0.141	0.696	0.608	0.608	0.619	0.617	0.608	0.623																																				
UniAD	0.888	0.912	0.888	0.875	0.839	0.842	0.809	0.801	0.863	0.877	0.849	0.838	0.711	0.729	0.720	0.710	0.537	0.614	0.578	0.575	0.455	0.527	0.512	0.513	0.602	0.748	0.722	0.728	0.528	0.700	0.610	0.610	0.567	0.664	0.639	0.637																																				
CS-FLOW	0.973	0.994	0.997	1.000	0.988	0.986	0.978	0.754	0.981	0.990	0.987	0.877	0.827	0.620	0.750	0.680	0.384	0.788	0.482	0.534	0.478	0.296	0.461	0.184	0.244	0.748	0.664	0.877	0.597	0.575	0.683	0.676	0.597	0.603	0.997	0.590	0.460																																			
CBFA	1.000	0.999	0.974	0.963	0.993	0.992	0.834	0.815	0.997	0.995	0.904	0.899	0.743	0.766	0.616	0.590	0.598	0.582	0.479	0.548	0.507	0.336	0.461	0.447	0.364	0.738	0.776	0.518	0.513	0.228	0.251	0.250	0.288	0.528	0.565	0.476	0.435																																			
DRAEM	0.704	0.700	0.656	0.677	0.951	0.980	0.897	0.836	0.927	0.984	0.976	0.757	0.643	0.673	0.590	0.607	0.767	0.742	0.790	0.784	0.467	0.476	0.338	0.384	0.546	0.537	0.460	0.507	0.572	0.640	0.542	0.521	0.598	0.613	0.544	0.563																																				
EfficientAD	0.861	0.778	0.894	0.896	1.000	0.995	1.000	1.000	0.920	0.886	0.947	0.973	0.768	0.745	0.539	0.673	0.579	0.552	0.524	0.578	0.431	0.448	0.413	0.413	0.815	0.865	0.648	0.691	0.313	0.324	0.278	0.337	0.581	0.543	0.480	0.538																																				
FastFlow	0.633	0.660	0.484	0.484	0.969	0.960	0.989	0.969	0.731	0.810	0.737	0.727	0.197	0.711	0.623	0.620	0.446	0.553	0.632	0.632	0.632	0.637	0.876	0.699	0.766	0.969	0.966	0.959	0.962	0.635	0.692	0.631	0.665	0.522	0.760	0.701	0.728																																			
Ganomaly	0.606	0.532	0.595	0.488	0.766	0.744	0.717	0.699	0.841	0.638	0.656	0.584	0.568	0.480	0.474	0.482	0.529	0.576	0.690	0.619	0.310	0.420	0.129	0.133	0.488	0.523	0.551	0.453	0.467	0.540	0.611	0.115	0.475	0.594	0.545	0.432																																				
STPFM	1.000	0.974	0.996	0.999	0.944	0.957	0.939	0.949	0.972	0.965	0.968	0.974	0.722	0.816	0.598	0.543	0.584	0.613	0.473	0.435	0.214	0.273	0.236	0.259	0.747	0.855	0.874	0.862	0.424	0.413	0.442	0.437	0.538	0.594	0.525	0.511																																				
CFLowAD	0.975	0.912	0.995	0.992	0.969	0.952	0.973	0.989	0.972	0.932	0.955	0.991	0.625	0.627	0.658	0.669	0.575	0.577	0.615	0.614	0.716	0.778	0.590	0.601	0.914	0.932	0.935	0.894	0.844	0.844	0.849	0.843	0.735	0.752	0.729	0.724																																				
DAE	0.924	0.953	0.790	0.815	0.478	0.467	0.487	0.493	0.701	0.710	0.639	0.654	0.467	0.475	0.350	0.351	0.614	0.601	0.508	0.415	0.785	0.923	0.606	0.553	0.713	0.725	0.701	0.698	0.835	0.790	0.773	0.796	0.683	0.703	0.587	0.581																																				
DFR	1.000	1.000	1.000	1.000	0.840	0.933	0.920	0.922	0.920	0.966	0.960	0.981	0.700	0.651	0.698	0.633	0.666	0.595	0.632	0.655	0.324	0.305	0.282	0.266	0.774	0.790	0.804	0.796	0.344	0.608	0.567	0.561	0.562	0.590	0.596	0.593																																				
PFI	0.904	0.890	0.941	0.942	0.490	0.632	0.470	0.598	0.697	0.761	0.706	0.725	0.597	0.402	0.424	0.424	0.633	0.739	0.546	0.560	0.801	0.836	0.734	0.734	0.472	0.697	0.295	0.366	0.753	0.897	0.899	0.866	0.675	0.714	0.580	0.598																																				
HTAES	0.903	0.921	0.897	0.899	0.881	0.833	0.918	0.889	0.982	0.877	0.907	0.974	0.832	0.792	0.685	0.689	0.529	0.555	0.765	0.750	0.605	0.777	0.260	0.154	0.438	0.669	0.510	0.343	0.449	0.385	0.378	0.561	0.631	0.636	0.519	0.612																																				
Reverse Distillation	0.985	0.985	0.968	0.971	0.985	0.985	0.968	0.971	0.987	0.985	0.968	0.971	0.471	0.526	0.459	0.459	0.537	0.647	0.658	0.607	0.762	0.745	0.557	0.588	0.893	0.951	0.960	0.951	0.821	0.778	0.832	0.858	0.688	0.729	0.693	0.693																																				
ShipGanomaly	0.865	0.984	0.991	0.916	0.872	0.967	0.956	0.952	0.869	0.976	0.978	0.884	0.369	0.347	0.355	0.360	0.406	0.394	0.430	0.423	0.637	0.665	0.689	0.576	0.602	0.418	0.326	0.345	0.620	0.625	0.625	0.634	0.527	0.490	0.485	0.468																																				
Average by epoch selection method	0.887	0.889	0.885	0.872	0.893	0.908	0.892	0.878	0.890	0.898	0.888	0.875	0.657	0.685	0.616	0.642	0.611	0.603	0.628	0.602	0.567	0.639	0.504	0.511	0.774	0.792	0.760	0.742	0.600	0.675	0.653	0.635	0.642	0.679	0.632	0.626																																				
Average by dataset	0.883				0.893				0.888				0.650				0.611			0.555				0.767				0.640				0.645																																								

TABLE IV
EXPERIMENT RESULTS (PR-AUC): IT SHOWS SIMILAR TRENDS TO ROC-AUC. EPOCHS SELECTED USING THE FULL VALIDATION SET ACHIEVED THE BEST PR-AUC, WHILE THE LOSS-BASED SELECTION PERFORMED SIMILARLY TO SAMPLE-WISE.

Dataset	Industrial Device Datasets												Real Pathology Images Datasets																														
	Hazelnut				Tile				Average				Glomerulus								Camelyon								Colon								S12						
Scale													512				2048				Camelyon				2048				S12				Average										
Best epoch	Sample	Val	Loss	Last	Sample	Val	Loss	Last	Sample	Val	Loss	Last	Sample	Val	Loss	Last	Sample	Val	Loss	Last	Sample	Val	Loss	Last	Sample	Val	Loss	Last	Sample	Val	Loss	Last	Sample	Val	Loss	Last							
DFM	0.995	0.995	0.995	0.995	0.992	0.992	0.992	0.992	0.993	0.993	0.993	0.993	0.624	0.624	0.624	0.624	0.855	0.855	0.855	0.855	0.503	0.503	0.503	0.503	0.995	0.995	0.995	0.995	0.788	0.788	0.788	0.788	0.753	0.753	0.753	0.753							
DFKDE	0.973	0.973	0.973	0.973	0.891	0.891	0.891	0.891	0.932	0.932	0.932	0.932	0.510	0.510	0.510	0.510	0.769	0.769	0.769	0.769	0.900	0.900	0.900	0.900	0.852	0.852	0.852	0.852	0.861	0.861	0.861	0.861	0.779	0.779	0.779	0.779							
PaDIM	0.981	0.981	0.981	0.981	0.804	0.804	0.804	0.804	0.893	0.893	0.893	0.893	0.488	0.488	0.488	0.488	0.715	0.715	0.715	0.715	0.337	0.337	0.337	0.337	0.684	0.684	0.684	0.684	0.643	0.643	0.643	0.643	0.573	0.573	0.573	0.573							
Patchcore	0.920	0.920	0.920	0.920	0.946	0.946	0.946	0.946	0.933	0.933	0.933	0.933	0.575	0.575	0.575	0.575	0.732	0.732	0.732	0.732	0.304	0.304	0.304	0.304	0.924	0.924	0.924	0.924	0.794	0.794	0.794	0.794	0.666	0.666	0.666	0.666							
Revisit Distillation	0.954	0.969	0.916	0.920	0.756	0.999	0.945	0.858	0.855	0.984	0.931	0.889	0.415	0.538	0.564	0.529	0.504	0.586	0.582	0.565	0.464	0.802	0.178	0.192	0.748	0.876	0.837	0.828	0.353	0.792	0.397	0.501	0.497	0.719	0.512	0.523							
PANDA	0.996	0.994	0.994	0.996	0.978	0.987	0.979	0.974	0.987	0.991	0.987	0.985	0.564	0.607	0.603	0.591	0.856	0.852	0.851	0.851	0.791	0.801	0.818	0.818	0.988	0.990	0.984	0.984	0.864	0.885	0.810	0.810	0.812	0.827	0.813	0.811							
IGD	0.982	0.988	0.983	0.984	0.971	0.913	0.972	0.975	0.976	0.950	0.977	0.979	0.582	0.531	0.537	0.612	0.732	0.795	0.657	0.668	0.826	0.761	0.486	0.467	0.744	0.827	0.651	0.643	0.982	0.998	0.998	0.983	0.773	0.783	0.666	0.675							
ReContrast	0.999	0.998	0.999	0.999	1.000	0.998	1.000	1.000	0.999	0.998	0.999	0.999	0.523	0.761	0.674	0.674	0.709	0.780	0.630	0.630	0.674	0.873	0.143	0.143	0.930	0.975	0.927	0.927	0.909	0.954	0.852	0.852	0.749	0.869	0.645	0.645							
UniAD	0.911	0.913	0.897	0.893	0.933	0.945	0.925	0.915	0.922	0.929	0.911	0.904	0.515	0.584	0.550	0.546	0.692	0.705	0.694	0.683	0.169	0.185	0.155	0.154	0.561	0.685	0.664	0.668	0.621	0.715	0.664	0.664	0.512	0.575	0.546	0.543							
CS-FLOW	0.995	0.997	0.989	0.825	0.984	1.000	0.998	1.000	0.989	0.998	0.994	0.912	0.720	0.556	0.913	0.452	0.677	0.798	0.308	0.406	0.209	0.252	0.214	0.161	0.736	0.504	0.875	0.543	0.547	0.698	0.811	0.735	0.578	0.561	0.624	0.459							
CFA	0.996	0.996	0.929	0.922	1.000	0.999	0.990	0.994	0.998	0.997	0.960	0.958	0.560	0.584	0.456	0.483	0.660	0.720	0.599	0.608	0.366	0.514	0.371	0.360	0.673	0.734	0.563	0.552	0.456	0.515	0.384	0.385	0.543	0.613	0.475	0.478							
DRAEM	0.973	0.991	0.949	0.922	0.876	0.873	0.831	0.806	0.924	0.932	0.890	0.864	0.764	0.709	0.773	0.761	0.591	0.557	0.545	0.602	0.489	0.442	0.254	0.260	0.508	0.511	0.504	0.554	0.523	0.610	0.531	0.527	0.575	0.566	0.521	0.541							
EfficientAD	1.000	0.997	1.000	1.000	0.935	0.894	0.949	0.951	0.967	0.946	0.974	0.975	0.556	0.578	0.568	0.558	0.745	0.710	0.549	0.666	0.254	0.287	0.287	0.287	0.802	0.595	0.699	0.718	0.393	0.457	0.377	0.404	0.550	0.525	0.496	0.527							
FastFlow	0.983	0.981	0.995	0.984	0.666	0.949	0.639	0.639	0.824	0.965	0.817	0.812	0.482	0.527	0.555	0.555	0.701	0.731	0.605	0.587	0.716	0.673	0.562	0.553	0.947	0.918	0.951	0.954	0.627	0.852	0.589	0.664	0.685	0.740	0.496	0.496							
GANomaly	0.782	0.884	0.804	0.849	0.773	0.712	0.795	0.706	0.778	0.798	0.799	0.777	0.531	0.555	0.625	0.539	0.518	0.484	0.698	0.788	0.274	0.357	0.144	0.134	0.530	0.575	0.562	0.488	0.600	0.619	0.633	0.326	0.491	0.518	0.532								
STFPM	0.952	0.954	0.951	0.938	1.000	0.987	0.998	1.000	0.976	0.970	0.975	0.969	0.575	0.602	0.451	0.479	0.732	0.637	0.593	0.544	0.210	0.273	0.170	0.203	0.698	0.846	0.816	0.817	0.472	0.462	0.462	0.474	0.537	0.564	0.498	0.504							
CFLow-AD	0.985	0.977	0.988	0.995	0.988	0.953	0.998	0.996	0.987	0.965	0.993	0.995	0.440	0.453	0.464	0.467	0.789	0.785	0.689	0.716	0.469	0.568	0.364	0.422	0.787	0.911	0.913	0.854	0.823	0.840	0.835	0.808	0.842	0.711	0.635								
DAE	0.926	0.899	0.715	0.719	0.975	0.974	0.890	0.903	0.951	0.936	0.803	0.811	0.534	0.565	0.549	0.759	0.685	0.716	0.550	0.631	0.420	0.697	0.431	0.323	0.673	0.826	0.667	0.651	0.814	0.784	0.776	0.801	0.625	0.717	0.595								
DFR	0.911	0.933	0.922	0.925	1.000	1.000	1.000	1.000	0.905	0.966	0.961	0.963	0.464	0.584	0.430	0.436	0.579	0.682	0.717	0.726	0.556	0.567	0.515	0.497	0.729	0.732	0.745	0.746	0.438	0.587	0.542	0.572	0.553	0.631	0.590								
FAE	0.684	0.870	0.669	0.681	0.937	0.912	0.967	0.967	0.810	0.891	0.818	0.824	0.490	0.528	0.537	0.527	0.581	0.659	0.627	0.642	0.749	0.615	0.584	0.584	0.464	0.648	0.382	0.407	0.700	0.836	0.878	0.831	0.597	0.657	0.602								
HTAES	0.949	0.920	0.967	0.945	0.954	0.963	0.947	0.934	0.952	0.942	0.957	0.939	0.745	0.599	0.787	0.776	0.792	0.785	0.724	0.850	0.306	0.653	0.158	0.340	0.456	0.606	0.489	0.410	0.451	0.403	0.410	0.549	0.550	0.609	0.514								
Reverse Distillation	0.954	0.969	0.916	0.920	0.756	0.999	0.945	0.858	0.855	0.984	0.931	0.889	0.415	0.538	0.564	0.529	0.504	0.586	0.582	0.565	0.464	0.802	0.178	0.192	0.748	0.876	0.837	0.828	0.353	0.792	0.397	0.501	0.497	0.719	0.512								
SkipGANomaly	0.939	0.982	0.963	0.973	0.918	0.992	0.996	0.903	0.929	0.987	0.989	0.938	0.422	0.416	0.433	0.429	0.419	0.406	0.417	0.414	0.266	0.280	0.254	0.232	0.594	0.628	0.632	0.626	0.636	0.640	0.640	0.648	0.467	0.474									
Average by epoch selection method	0.941	0.960	0.932	0.924	0.914	0.943	0.930	0.914	0.928	0.951	0.931	0.919	0.543	0.566	0.575	0.561	0.676	0.698	0.639	0.661	0.468	0.541	0.361	0.364	0.729	0.770	0.746	0.724	0.631	0.719	0.655	0.657	0.609	0.659									
Average by dataset	0.939				0.925				0.932				0.561				0.668				0.433				0.742				0.666				0.614										

C. Limitations

This work has some limitations. To ensure consistent coverage between small-scale and large-scale patches, we used the default parameters provided in the program, which limited the number of large-scale patches used for training. Additionally, due to time and resource constraints, we were unable to fine-tune the model for each dataset. Instead, we used the default parameters uniformly across all datasets.

VI. CONCLUSIONS

This review provides an extensive benchmark of 23 anomaly detection methods applied to digital pathology images, highlighting both their potential and limitations. Through evaluations on diverse real and synthetic datasets, we reveal that no single method consistently outperforms others, and performance is highly dependent on image scale, anomaly patterns, and training strategies. Our findings underscore the need for pathology-specific designs and robust evaluation protocols, offering valuable insights to guide future research in this emerging field.

ACKNOWLEDGMENT

This work was supported by the National Institutes of Health under award numbers R01DK135597 (Huo), R01EB033385, R01DK132338, REB017230, R01MH125931, and R01DK128200 (KTW), DoD HT9425-23-1-0003 (HCY), and KPMP Glue Grant. This study was also supported by the National Science Foundation (2040462). This work was also supported by NSF NAIRR Pilot Award NAIRR240055. This project was also supported by The Leona M. and Harry B. Helmsley Charitable Trust grant G-1903-03793 and G-2103-05128. This research was also supported by Veterans Affairs Merit Review grants I01CX002662, I01CX002171 (KTW), and I01CX002473 (KTW). This work was also supported by Vanderbilt Seed Success Grant, Vanderbilt Discovery Grant, and VISE Seed Grant. We extend gratitude to NVIDIA for their support by means of the NVIDIA hardware grant.

REFERENCES

- [1] J. Liu, G. Xie, J. Wang, S. Li, C. Wang, F. Zheng, and Y. Jin, "Deep industrial image anomaly detection: A survey," *Machine Intelligence Research*, vol. 21, no. 1, pp. 104–135, 2024.
- [2] A. B. Nassif, M. A. Talib, Q. Nasir, and F. M. Dakalbab, "Machine learning for anomaly detection: A systematic review," *Ieee Access*, vol. 9, pp. 78 658–78 700, 2021.
- [3] Q. Gu, C. Meroueh, J. Levernier, T. Kroneman, T. Flotte, and S. Hart, "Using an anomaly detection approach for the segmentation of colorectal cancer tumors in whole slide images," *Journal of Pathology Informatics*, vol. 14, p. 100336, 2023.
- [4] I. Zingman, B. Stierstorfer, C. Lempp, and F. Heinemann, "Learning image representations for anomaly detection: application to discovery of histological alterations in drug development," *Medical Image Analysis*, vol. 92, p. 103067, 2024.
- [5] L. Shelton, R. Soans, T. Shah, T. Forest, K. Janardhan, M. Napolitano, R. Gonzalez, G. Carlson, J. K. Shah, and A. Chen, "Automated anomaly detection in histology images using deep learning," in *Medical Imaging 2024: Digital and Computational Pathology*, vol. 12933. SPIE, 2024, pp. 152–158.
- [6] Y. Cui, Z. Liu, and S. Lian, "A survey on unsupervised anomaly detection algorithms for industrial images," *IEEE Access*, vol. 11, pp. 55 297–55 315, 2023.
- [7] Y. Cao, X. Xu, J. Zhang, Y. Cheng, X. Huang, G. Pang, and W. Shen, "A survey on visual anomaly detection: Challenge, approach, and prospect," *arXiv preprint arXiv:2401.16402*, 2024.
- [8] Y. Cai, W. Zhang, H. Chen, and K.-T. Cheng, "Medianomaly: A comparative study of anomaly detection in medical images," *Medical Image Analysis*, p. 103500, 2025.
- [9] I. Lagogiannis, F. Meissen, G. Kaissis, and D. Rueckert, "Unsupervised pathology detection: a deep dive into the state of the art," *IEEE transactions on medical imaging*, vol. 43, no. 1, pp. 241–252, 2023.
- [10] J. Bao, H. Sun, H. Deng, Y. He, Z. Zhang, and X. Li, "Bmad: Benchmarks for medical anomaly detection," in *Proceedings of the IEEE/CVF Conference on Computer Vision and Pattern Recognition*, 2024, pp. 4042–4053.
- [11] Z. You, L. Cui, Y. Shen, K. Yang, X. Lu, Y. Zheng, and X. Le, "A unified model for multi-class anomaly detection," *Advances in Neural Information Processing Systems*, vol. 35, pp. 4571–4584, 2022.
- [12] V. Zavrtanik, M. Kristan, and D. Škočaj, "Draem-a discriminatively trained reconstruction embedding for surface anomaly detection," in *Proceedings of the IEEE/CVF international conference on computer vision*, 2021, pp. 8330–8339.
- [13] Y. Chen, Y. Tian, G. Pang, and G. Carneiro, "Deep one-class classification via interpolated gaussian descriptor," in *Proceedings of the AAAI Conference on Artificial Intelligence*, vol. 36, no. 1, 2022, pp. 383–392.
- [14] A. Kascenas, N. Pugeault, and A. Q. O'Neil, "Denoising autoencoders for unsupervised anomaly detection in brain mri," in *International Conference on Medical Imaging with Deep Learning*. PMLR, 2022, pp. 653–664.
- [15] J. Silva-Rodríguez, V. Naranjo, and J. Dolz, "Constrained unsupervised anomaly segmentation," *Medical Image Analysis*, vol. 80, p. 102526, 2022.
- [16] S. Akcay, A. Atapour-Abarghouei, and T. P. Breckon, "Ganomaly: Semi-supervised anomaly detection via adversarial training," in *Computer Vision—ACCV 2018: 14th Asian Conference on Computer Vision, Perth, Australia, December 2–6, 2018, Revised Selected Papers, Part III 14*. Springer, 2019, pp. 622–637.
- [17] F. Meissen, J. Paetzold, G. Kaissis, and D. Rueckert, "Unsupervised anomaly localization with structural feature-autoencoders," in *International MICCAI Brainlesion Workshop*. Springer, 2022, pp. 14–24.
- [18] J. Yang, Y. Shi, and Z. Qi, "Dfr: Deep feature reconstruction for unsupervised anomaly segmentation," *arXiv preprint arXiv:2012.07122*, 2020.
- [19] A. Ghorbel, A. Aldahdooh, S. Albarqouni, and W. Hamidouche, "Transformer based models for unsupervised anomaly segmentation in brain mr images," in *International MICCAI Brainlesion Workshop*. Springer, 2022, pp. 25–44.
- [20] T. Reiss, N. Cohen, L. Bergman, and Y. Hoshen, "Panda: Adapting pretrained features for anomaly detection and segmentation," in *Proceedings of the IEEE/CVF Conference on Computer Vision and Pattern Recognition*, 2021, pp. 2806–2814.
- [21] K. Roth, L. Pemula, J. Zepeda, B. Schölkopf, T. Brox, and P. Gehler, "Towards total recall in industrial anomaly detection," in *Proceedings of the IEEE/CVF conference on computer vision and pattern recognition*, 2022, pp. 14 318–14 328.
- [22] S. Lee, S. Lee, and B. C. Song, "Cfa: Coupled-hypersphere-based feature adaptation for target-oriented anomaly localization," *IEEE Access*, vol. 10, pp. 78 446–78 454, 2022.
- [23] "DFKDE - Anomalib Documentation," <https://anomalib.readthedocs.io/en/latest/markdown/guides/reference/models/image/dfkde.html>.
- [24] N. A. Ahuja, I. Ndiour, T. Kalyanpur, and O. Tickoo, "Probabilistic modeling of deep features for out-of-distribution and adversarial detection," *arXiv preprint arXiv:1909.11786*, 2019.
- [25] T. Defard, A. Setkov, A. Loesch, and R. Audigier, "Padim: a patch distribution modeling framework for anomaly detection and localization," in *International conference on pattern recognition*. Springer, 2021, pp. 475–489.
- [26] H. Deng and X. Li, "Anomaly detection via reverse distillation from one-class embedding," in *Proceedings of the IEEE/CVF conference on computer vision and pattern recognition*, 2022, pp. 9737–9746.
- [27] T. D. Tien, A. T. Nguyen, N. H. Tran, T. D. Huy, S. Duong, C. D. T. Nguyen, and S. Q. Truong, "Revisiting reverse distillation for anomaly detection," in *Proceedings of the IEEE/CVF conference on computer vision and pattern recognition*, 2023, pp. 24 511–24 520.

- [28] G. Wang, S. Han, E. Ding, and D. Huang, "Student-teacher feature pyramid matching for anomaly detection," *arXiv preprint arXiv:2103.04257*, 2021.
- [29] J. Guo, S. Lu, L. Jia, W. Zhang, and H. Li, "Recontrast: Domain-specific anomaly detection via contrastive reconstruction," *Advances in Neural Information Processing Systems*, vol. 36, pp. 10721–10740, 2023.
- [30] J. Yu, Y. Zheng, X. Wang, W. Li, Y. Wu, R. Zhao, and L. Wu, "Fastflow: Unsupervised anomaly detection and localization via 2d normalizing flows," *arXiv preprint arXiv:2111.07677*, 2021.
- [31] D. Gudovskiy, S. Ishizaka, and K. Kozuka, "Cflow-ad: Real-time unsupervised anomaly detection with localization via conditional normalizing flows," in *Proceedings of the IEEE/CVF winter conference on applications of computer vision*, 2022, pp. 98–107.
- [32] M. Rudolph, T. Wehrbein, B. Rosenhahn, and B. Wandt, "Fully convolutional cross-scale-flows for image-based defect detection," in *Proceedings of the IEEE/CVF winter conference on applications of computer vision*, 2022, pp. 1088–1097.
- [33] C.-L. Li, K. Sohn, J. Yoon, and T. Pfister, "Cutpaste: Self-supervised learning for anomaly detection and localization," in *Proceedings of the IEEE/CVF conference on computer vision and pattern recognition*, 2021, pp. 9664–9674.
- [34] N. Shvetsova, B. Bakker, I. Fedulova, H. Schulz, and D. V. Dylov, "Anomaly detection in medical imaging with deep perceptual autoencoders," *IEEE Access*, vol. 9, pp. 118 571–118 583, 2021.
- [35] P. Zehnder, J. Feng, R. N. Fuji, R. Sullivan, and F. Hu, "Multiscale generative model using regularized skip-connections and perceptual loss for anomaly detection in toxicologic histopathology," *Journal of Pathology Informatics*, vol. 13, p. 100102, 2022.
- [36] M. Pocevičiūtė, G. Eilertsen, and C. Lundström, "Unsupervised anomaly detection in digital pathology using gans," in *2021 IEEE 18th International Symposium on Biomedical Imaging (ISBI)*. IEEE, 2021, pp. 1878–1882.
- [37] J. Johnson, A. Alahi, and L. Fei-Fei, "Perceptual losses for real-time style transfer and super-resolution," in *Computer Vision—ECCV 2016: 14th European Conference, Amsterdam, The Netherlands, October 11–14, 2016, Proceedings, Part II 14*. Springer, 2016, pp. 694–711.
- [38] S. Akcay, A. Atapour-Abarghouei, and T. P. Breckon, "Ganomaly: Semi-supervised anomaly detection via adversarial training," in *Asian conference on computer vision*. Springer, 2018, pp. 622–637.
- [39] Y.-C. Lai and W.-T. Chu, "Unsupervised anomaly detection on histopathology images using adversarial learning and simulated anomaly," in *Annual Conference on Medical Image Understanding and Analysis*. Springer, 2024, pp. 357–371.
- [40] J. Linmans, G. Raya, J. van der Laak, and G. Litjens, "Diffusion models for out-of-distribution detection in digital pathology," *Medical Image Analysis*, vol. 93, p. 103088, 2024.
- [41] G. Litjens, P. Bandi, B. Ehteshami Bejnordi, O. Geessink, M. Balkenhol, P. Bult, A. Halilovic, M. Hermsen, R. van de Loo, R. Vogels *et al.*, "1399 h&e-stained sentinel lymph node sections of breast cancer patients: the camelyon dataset," *GigaScience*, vol. 7, no. 6, p. giy065, 2018.
- [42] B. E. Bejnordi, M. Veta, P. J. Van Diest, B. Van Ginneken, N. Karssemeijer, G. Litjens, J. A. Van Der Laak, M. Hermsen, Q. F. Manson, M. Balkenhol *et al.*, "Diagnostic assessment of deep learning algorithms for detection of lymph node metastases in women with breast cancer," *Jama*, vol. 318, no. 22, pp. 2199–2210, 2017.
- [43] S. Bao, S. Chiron, Y. Tang, C. N. Heiser, A. N. Southard-Smith, H. H. Lee, M. A. Ramirez, Y. Huo, M. K. Washington, E. A. Scoville *et al.*, "A cross-platform informatics system for the gut cell atlas: integrating clinical, anatomical and histological data," in *Medical Imaging 2021: Imaging Informatics for Healthcare, Research, and Applications*, vol. 11601. SPIE, 2021, pp. 8–15.
- [44] T. Yao, Y. Lu, J. Long, A. Jha, Z. Zhu, Z. Asad, H. Yang, A. B. Fogo, and Y. Huo, "Glo-in-one: holistic glomerular detection, segmentation, and lesion characterization with large-scale web image mining," *Journal of Medical Imaging*, vol. 9, no. 5, pp. 052408–052408, 2022.
- [45] C. A. Barbano, D. Perlo, E. Tartaglione, A. Fiandrotti, L. Bertero, P. Cassoni, and M. Grangetto, "Unitopatho, a labeled histopathological dataset for colorectal polyps classification and adenoma dysplasia grading," in *2021 IEEE International Conference on Image Processing (ICIP)*. IEEE, 2021, pp. 76–80.
- [46] P. Bergmann, M. Fauser, D. Sattlegger, and C. Steger, "Mvtec ad—a comprehensive real-world dataset for unsupervised anomaly detection," in *Proceedings of the IEEE/CVF conference on computer vision and pattern recognition*, 2019, pp. 9592–9600.
- [47] C. Cui, Y. Wang, S. Bao, Y. Tang, R. Deng, L. W. Remedios, Z. Asad, J. T. Roland, K. S. Lau, Q. Liu *et al.*, "Feasibility of universal anomaly detection without knowing the abnormality in medical images," in *Workshop on Medical Image Learning with Limited and Noisy Data*. Springer, 2023, pp. 82–92.
- [48] S. Akçay, A. Atapour-Abarghouei, and T. P. Breckon, "Skip-ganomaly: Skip connected and adversarially trained encoder-decoder anomaly detection," in *2019 International Joint Conference on Neural Networks (IJCNN)*. IEEE, 2019, pp. 1–8.